Chapter 8
Computational Fluid Dynamics for the Assessment of Cerebrospinal Fluid Flow and Its Coupling with Cerebral Blood Flow

Vartan Kurtcuoglu

8.1 Introduction

The dynamics of cerebrospinal fluid flow are directly linked to those of the cardiovascular system. The heart not only drives blood flow, but is also at the origin of CSF pulsation through the expansion and contraction of cerebral blood vessels. As was detailed in the preceding chapter, CSF dynamics can be altered by diseases and conditions such as hydrocephalus and, in turn, CSF dynamics can be analyzed to aid in the diagnosis of these. Bulk models describing intracranial fluid dynamics and punctual flow measurements using MRI have thus become important tools for this purpose.

The strength of bulk models is that they are computationally inexpensive. Simulations performed with such models and processing of the results generally do not require high-performance computing (HPC) resources and can be carried out very quickly on common personal computers. This is currently a prerequisite for application in clinical settings, where typically no access to HPC infrastructure is available. In terms of applicability, the hunger for computer power is the main differentiator between bulk models and computational fluid dynamics (CFD) models of intracranial dynamics. Unlike the bulk approach, however, CFD models can provide spatially resolved information on flow, pressure and mass transport, which opens the door to subject-specific calculations of intracranial dynamics based on medical imaging data. This chapter elucidates current approaches to CFD modeling of cerebrospinal fluid flow and its interaction with blood flow.

The development of CFD was driven by the lack of analytical solutions for the Navier–Stokes (NS) equations that describe momentum conservation in Newtonian

V. Kurtcuoglu (✉)
Laboratory of Thermodynamics in Emerging Technologies, Department of Mechanical and Process Engineering, ETH Zurich, Sonneggstrasse 3, ML J 27.2 8092 Zurich, Switzerland
e-mail: vartan.kurtcuoglu@ethz.ch

K. Miller (ed.), *Biomechanics of the Brain*, Biological and Medical Physics, Biomedical Engineering, DOI 10.1007/978-1-4419-9997-9_8,

fluids. Together with the continuity equation, i.e. the expression of mass conservation and energy conservation, the NS equations can be used to characterize continuum flows. For incompressible flows without external body forces, Equations (8.1) and (8.2) show the NS and continuity equations, respectively:

$$\rho\left(\frac{\partial u}{\partial t} + u \cdot \nabla u\right) = -\nabla p + \mu \nabla^2 u \tag{8.1}$$

$$\nabla \cdot u = 0. \tag{8.2}$$

Here, ρ is density, u is the velocity vector, t is time, p is pressure and μ is dynamic viscosity.

CFD simulations in the CSF system started in 1996 with the work of Jacobsen et al. [1]. This is quite late compared to CFD work on blood flow that began in the early 1970s and can be attributed to both the fact that the cardiovascular system is better known to the non-medical public (which includes the engineers, mathematicians and physicists who develop CFD methods and search for applications of these) and to the anatomically more complex structure of the CSF space that cannot be easily reduced to 2D representations. The widespread availability of magnetic resonance imaging systems in medical research institutions at the turn of the century was a prerequisite for the transition from generic to subject-specific, anatomically accurate computational models, and thereby paved the way for CFD simulations of flow in the CSF space.

The procedural steps in the CFD modeling of cerebrospinal fluid flow are similar to those encountered in more generic problems of incompressible, isothermal internal flows: In a first step, the simulation domain has to be defined, which consists of at least one fluid domain and, if the deformation of surrounding tissue is to be modeled, one or more solid domains. In the second step, these domains have to be discretized, i.e. a spatial discretization scheme needs to be chosen and a computational grid has to be generated. Next, the behavior of the fluids and solids at their respective domain boundaries needs to be prescribed, i.e. corresponding pressures, velocities or their derivatives in those areas must be determined a priori and set accordingly. In the fourth step, the physical properties of the fluids and solids (rheology, material properties) have to be set. Finally, the NS and continuity equations have to be solved based on appropriate initial conditions. If the problem is transient, a suitable temporal discretization scheme is required for this. The following section discusses these steps for the case of subject-specific CSF flow simulations based on MRI data.

8.2 Procedural Steps in CFD Modeling of CSF Dynamics

8.2.1 Obtaining the Model Domain

Magnetic resonance imaging is the most widely used method for obtaining representations of the CSF spaces as well as of arterial blood vessels in the head. However, the effective obtainable resolution is limited by comparably slow acquisition times

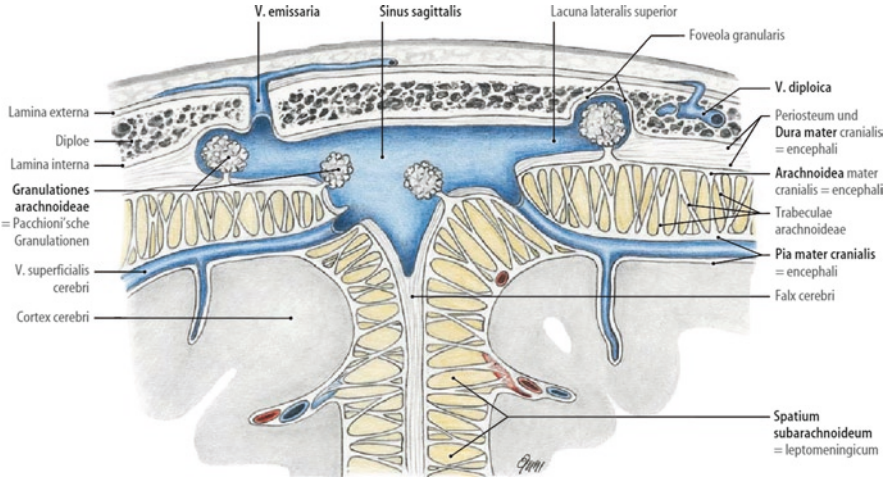

Fig. 8.1 Schematic of the subarachnoid space (spatium subarachnoideum) in the vicinity of the superior sagittal sinus. Trabeculae connect the arachoid and pia membranes (arachnoidea mater cranials, pia mater cranialis). From Tillmann [57]

combined with the fact that the brain moves inadvertently due to cardiac pulsation and breathing. Consequently, the largest part of the cerebral vasculature cannot be acquired in sufficient detail for modeling with CFD. If the coupling between blood and cerebrospinal fluid flow is to be taken into account explicitly by calculating the transient displacements of the arterial walls and their transmission to the CSF space, then smaller vessels have to be simulated via lower order models. The representation of the smaller vessels can then be coupled to full 3D CFD models of larger vessels, such as the internal carotid arteries, vertebral arteries, basilar artery and the circle of Willis (see Figs. 2.17 and 2.21 in Chap. 2). Similar limitations with respect to the effective resolution of MRI also affect the CSF space directly: Structures such as small diameter sections of the foramina of Monroe, Luschka and Magendie, the posterior horns of the lateral ventricles, the aqueduct of Sylvius and the recesses of the third and fourth ventricle (see Fig. 2.7, Chap. 2) will be substantially affected by partial volume effects [2]. Nevertheless, the overall feature size of these structures is large enough that lower order modeling is not required. In contrast, the subarachnoid space (SAS) features a micro-scale substructure that is well below the resolution limit of clinical MRI systems even in the absence of brain motion: Fine filaments (trabeculae) with diameters in the double digit micron range bridge the SAS between the pia and arachnoid membranes (Fig. 8.1). Despite their small size, the trabeculae may increase the pressure drop along the SAS significantly [3, 4]. Consequently, their effect on CSF flow and associated mass transport should be taken into account, e.g. by approximating the trabecular network as a porous medium with specified permeability [3]. Unfortunately, there is no experimental data on the permeability of the SAS. Thus, SAS porosity has to be obtained first, wherefrom permeability values can be derived. The best description of the trabecular structure for the purpose of deriving porosity

can be found in analyses of electron microscopy acquisitions [5–7]. Once porosity is determined, permeability can be estimated through CFD or analytical exploration in an idealized SAS representation, most likely the simplest of which is an array of straight circular cylinders connecting two parallel plates that represent the pia and arachnoid layer [8]. For this case, the relationship between porosity and permeability is given by

$$\frac{k_l}{r^2} = \frac{\varepsilon^2(\pi + 2.157(1-\varepsilon))}{48(1-\varepsilon)^2} \quad \text{and} \quad \frac{k_t}{r^2} = \frac{\pi\varepsilon(1-\sqrt{1-\varepsilon})^2}{24(1-\varepsilon)^{3/2}}, \tag{8.3}$$

where k_l is longitudinal permeability (i.e. permeability in direction parallel to the cylinders representing the trabeculae), k_t is transverse permeability, r is the radius of the cylinders and ε is the porosity of the SAS. The flow resistance caused by the porous micro-structure of the SAS can then be accounted for by the addition of a pressure gradient to the right hand side of the NS equations, e.g. for a coordinate system aligned with the direction of the trabeculae:

$$\rho\left(\frac{\partial u}{\partial t} + u\cdot\nabla u\right) = -\nabla p + \mu\nabla^2 u - \mu\begin{pmatrix} u_1/k_l \\ u_2/k_t \\ u_3/k_t \end{pmatrix}. \tag{8.4}$$

Equation (8.4) is valid if inertial losses due to the porous micro-structure are small compared to its viscous drag, i.e. if the Reynolds number with trabecular diameter as characteristic length is smaller than 0.5 [9]. This is presumably the case in the SAS [3], but more accurate information on trabecular geometry and configuration is needed to validate this finding. When blood vessels in the SAS are considered as well, inertial losses will become important. However, these vessels cannot be treated as part of the homogeneous trabecular micro-structure, but could be introduced within the framework of a multi-scale porous model. While this has not been attempted in the CSF space, there are examples of comparable models in other application areas [10].

After MR images of the central nervous system are acquired, the anatomical structures that are to be included in the CFD model need to be extracted, i.e. image segmentation has to be performed. Various algorithms exist for the automatic segmentation of larger vessels [11]. Some manual post-processing for the removal of artefacts is often required before the next steps in the CFD analysis chain can be performed. For the CSF space, much lower quality results can be expected from automatic segmentation. While some algorithms exist that deliver automatic results for visualization and crude calculation purposes, these do not reach the quality required for accurate CFD simulations even after manual clean-up. Consequently, semi-automatic segmentation of the CSF domain is necessary. This is arduous, time consuming and poses severe limitations on the applicability of CFD for clinical CSF flow simulations.

The output of the segmentation step is a volumetric representation of the anatomical structures of interest. For CFD modeling, a distinction needs to be made between the internal fluid region and its boundaries. This is generally achieved by

surface triangulation [12]. The triangulation step is straightforward and can be carried out by various open source and commercial programs. As an alternative to segmentation and triangulation, splines [13] can be used to delineate the contour of the structure of interest in each MRI slide, followed by a surface reconstruction step that smoothly joins the splines to an approximation of the respective boundary. Surface reconstruction can also be performed after triangulation, which combines the benefits of voxel-based segmentation (preservation of original shape details) with those of spline description (scalability, small file size, best template for computational grid generation). The disadvantage is that surface reconstruction of complex triangulated surfaces requires substantial manual work.

It is common in classical CFD applications to reduce the size of the fluid domain by making use of symmetries, or by reducing a 3D structure to a 2D representation. The latter can be used, for example, to investigate the performance of airplane wings, where instead of calculating the flow around the entire 3D profile, only the flow around an axial cross-section (airfoil) would be considered. While tip effects and interactions with the airplane fuselage cannot be studied in this way, the approach is nonetheless permissible, since there is only limited flow perpendicular to the axial section. It is more difficult to find viable reductions of dimension for use within the CSF space. One might consider conducting a 2D CFD study on the third ventricle limited to its mid-sagittal plane. However, the inlets to this ventricle, the foramina of Monro, are located outside the mid-sagittal plane and their center lines are angled towards it, causing considerable CSF flow through this plane. Similarly, representing the cranial SAS by a 2D projection to its mid-sagittal plane is not permissible: The foramina of Luschka – two of the pathways connecting the ventricular space with the SAS – are not located in the mid-sagittal plane. The situation is better in the spinal SAS, where subsections with limited curvature and thus little flow perpendicular to the longitudinal axis exist (discounting substructures such as nerves and trabeculae). Flow in the perivascular space (extension of the SAS along blood vessels [14]) can most likely be simplified to 2D as well, although very little is known about fluid flow therein.

8.2.2 Spatial Discretization

CFD requires the discretization of the governing equations in space and, if transient flows are to be studied, also in time. For spatial discretization, the domain under investigation has to be divided into small sub-volumes, i.e. a computational grid has to be generated. The structure of this grid will depend on the expected characteristics of the flow and on the discretization methods to be applied. For the study of CSF dynamics, the finite-volume discretization scheme is used most often, followed by the finite-element method, although other approaches are principally just as suitable. When anatomically accurate modeling of the CSF flow is carried out, either unstructured grids or an immersed boundary method [15] need to be used, as structured grids that follow the domain contours are very difficult to generate due to the geometric complexity of the CSF spaces. State-of-the-art grid generation software

allows for mostly automatic unstructured meshing, usually with tetrahedral elements. Hexahedral elements that are commonly used in structured grids offer higher solution accuracy at the same overall number of elements, but they often necessitate buffer elements (pyramids, prisms and tetrahedra) in areas of high grid density gradients, increasing the complexity of grid generation. Prismatic buffer elements are also used in conjunction with otherwise tetrahedral grids in boundary layer areas, where high velocity gradients need to be resolved. Less common but emerging are polyhedral grids that can be generated with the same level of automation as tetrahedral grids, while offering more accurate solutions [16].

It is evident that by solving the discretized versions of the NS and continuity equations, only an approximate solution of the original set of governing equations is obtained. The quality of the approximation is, among other factors, dependent on the quality of the computational grid. Since the original solution is not known and, thus, the relative error of the discretized solution cannot be specified, solutions obtained with different grids have to be compared. Such grid independence studies will give an estimate of the relative error introduced by the spatial discretization. Ultimately, a balance between the accuracy of the results and cost in terms of grid generation and computational time has to be found.

8.2.3 Obtaining Boundary Conditions

Boundary conditions (BC) need to be specified at the domain margins for closure of the governing equations. CFD models of CSF flow are generally set up with BC based on MRI data. Unfortunately, it is not possible to obtain absolute pressures via MRI. This leads to the unsatisfactory situation that only velocity, flow rate or similar BC can be prescribed in a subject-specific manner, while pressure or impedance BC that are required to ensure mass conservation in non-compliant domains are generic or based on generalized lower order models.

The ideal locations for acquisition of flow BC in the CSF space are the aqueduct of Sylvius and the cervical spinal canal. The geometry of these areas is well defined and velocities therein are mostly limited to the axial direction, allowing for the placement of a single perpendicular measurement plane. Furthermore, there are closed-form solutions of flow in idealized representations of the aqueduct (e.g. straight elliptic pipe [17]) and the spinal canal (straight elliptic annulus [18]), allowing for the filtering of higher frequency noise components in the acquired flow data. This can be done by first integrating the flow profile in space for each measured point in time which yields a volumetric or mass flow curve that contains less random noise. In order to recuperate the spatial distribution of the flow, this flow rate is applied to the respective idealized geometry with available closed-form solution of the governing equations [19]. Finally, conformal mapping is performed to map the solution back to the actual domain [20].

Pulsatile CSF flow is driven by the expansion and contraction of blood vessels in and around the central nervous system, as well as by diaphragm motion in the

Fig. 8.2 Corrosion cast of the head and neck vasculature of a human cadaver. Image courtesy of Axel Lang (corrosion casting) and Heinz Sonderegger (photography). Copyright Institute of Anatomy, University of Zurich, Switzerland

abdominal space due to breathing. This means that the boundaries of the CSF compartments have to be flexible entities that can transfer momentum by deformation. Most existing CFD models assume nevertheless rigid CSF domain boundaries, as this simplifies model setup and calculations tremendously. There are two general approaches by which the motion of the CSF boundaries can be taken into account: Either the entire chain of displacements from blood vessels or the diaphragm to tissue and CSF domain boundaries is modeled, or the displacement of the boundaries is measured directly. The former approach poses great challenges, the most serious of which is the lack of material data to realistically model the interaction between blood vessels or the diaphragm and the surrounding tissue. In addition, the complexity of the vascular network in the brain (see Fig. 8.2) as well as limits in the effective resolution of MRI require simplifications of the vascular model (see Sect. 8.2.1), introducing errors that are difficult to quantify.

Measuring the motion of the CSF space boundaries directly is not straightforward, but it is feasible: Displacement-encoded MR imaging can detect brain displacements down to 0.01 mm [21] (Fig. 8.3), which is sufficient to derive ventricle wall motion, but not necessarily the motion of the pia mater. The MRI acquisitions result in a discrete displacement map within which the CSF boundaries do not necessarily coincide with the measured locations. Hence, a spatial interpolation has to be performed first to cover the boundaries. Since the temporal frequency spectrum

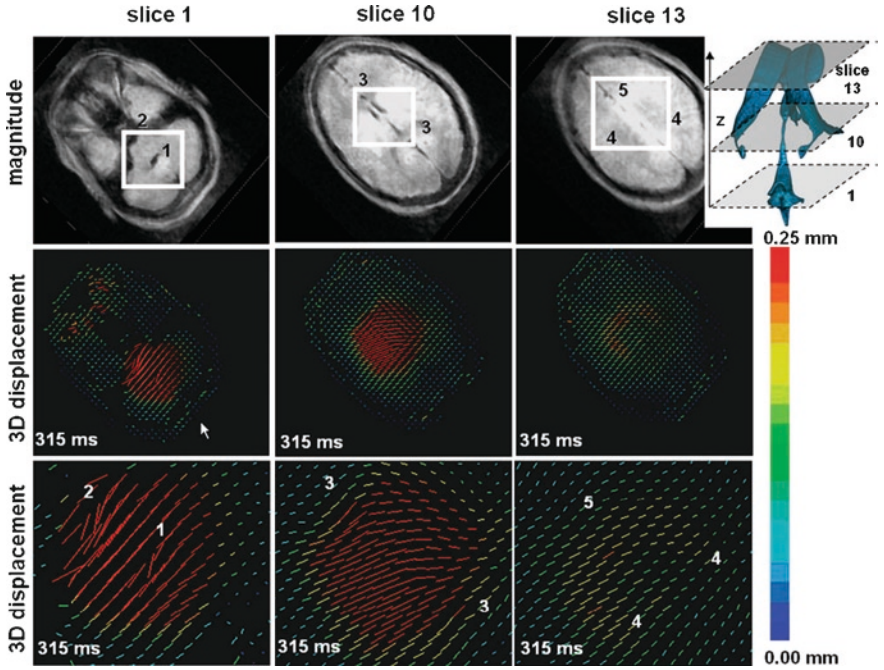

Fig. 8.3 Selected slices of a 3D brain motion data set covering the volume of the ventricular system [21]. The locations of the slices are indicated in the *upper right corner* with respect to the ventricular system of the brain. The *colors* and the *length* (scaled by a factor of 100) of the bars represent the motion amplitude of the brain, and the *bar orientation* indicates the displacement direction

of blood flow into the brain through the carotid and vertebral arteries does not extend beyond 10 Hz under normal resting conditions (Fig. 8.4), a brain motion acquisition interval of 0.05 s within a cardiac cycle is sufficient to meet the Nyquist–Shannon sampling criterion [22, 23]. However, the temporal discretization of the governing equations requires much smaller time steps, which necessitates a temporal interpolation of the acquired brain motion data. This can be done, for example, by Fourier decomposition of the acquired discrete signal and re-sampling of the reconstructed continuous signal [19].

Both ventricle wall motion and transient displacement of the pia mater transfer momentum to the CSF and thus contribute to its pulsation. Even a small displacement of the pia mater will result in substantial volume flow due to its large surface area. Thus, pia motion cannot be neglected. Since, as mentioned, MR imaging cannot capture the displacement of the pia mater, a simplified BC has to be introduced. One option is to prescribe uniform perpendicular flow across the pia, such that the corresponding flow rate is equal to the difference between in- and outflow at the aqueduct of Sylvius and the spinal canal [4]. This simplified BC is relatively easy to implement, but will lead to errors in the reported flow velocities close to the pia surface.

The pulsatile motion of CSF is superimposed onto its steady flow caused by production in the choroid plexus and absorption in the arachnoid granulations,

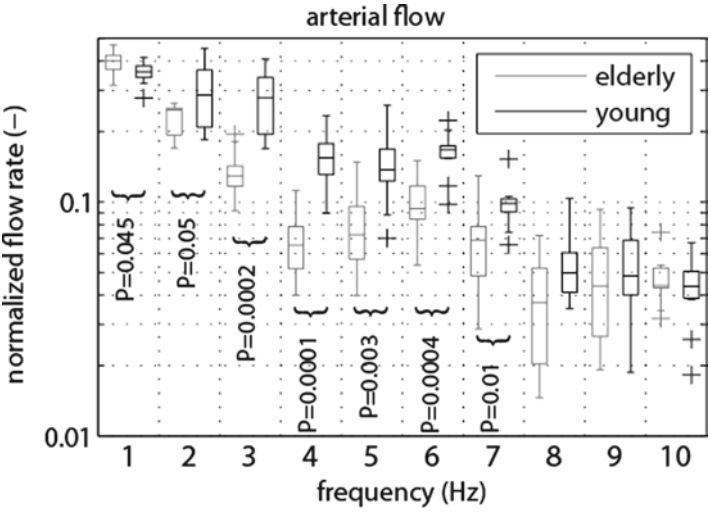

Fig. 8.4 Frequency spectrum of combined carotid and vertebral arterial blood flow in 11 elderly (*gray*, *left*, mean age 70 ± 5 years) and 11 young (*black*, *right*, mean age 24 ± 3 years) healthy subjects illustrated using *boxplots* [58]. The *upper* and *lower edges* of each box represent the 25th and 75th percentiles, respectively. The *center line* represents the median and the whiskers extend to the most extreme data points not considered outliers, which are plotted individually (+). *Curly brackets* indicate significant differences (non-parametric Mann–Whitney test). Distinction between signal and noise is not possible at frequencies beyond 7 Hz

extra-cranial lymphatic pathways and possibly through cerebral capillaries [24]. The choroid plexus has a filamentous structure that cannot be acquired by MRI in its full detail. For CFD modeling, its simplified macroscopic shape can be segmented from MR images and CSF flow rates corresponding to the production value can be imposed on the idealized boundaries. Alternatively, the choroid plexus geometry can be neglected altogether and inflow imposed at a part of the respective ventricle wall. Combined CSF production rates in the choroid plexus of the third and lateral ventricles can, principally, be obtained by integrating the MRI-acquired CSF flow profile in the aqueduct of Sylvius over a cardiac cycle. While this method is used throughout the literature, there is not conclusive data on the accuracy of this approach. Obtaining CSF production rates in the fourth ventricle via MRI is more difficult and would require measurement of flow through the small foramina of Luschka and Magendie. This is not possible with a sufficient level of accuracy on current clinical MRI scanners. In order to still take CSF production in the fourth ventricle into account, a ratio between the production rates in this and the remaining cerebral ventricles can be assumed.

Under physiological conditions, the average CSF absorption rate is equal to the respective production rate. CSF absorption locations are distributed throughout the cranial and spinal cavity, and there is no consensus on the relative importance of the various pathways, let alone on the actual drainage rates through each [25]. The classically accepted locations of CSF re-absorption are the arachnoid granulations (AG) that drain into the superior sagittal, transverse and sigmoid sinuses. It is possible

to locate large AG through MRI, but most of the smaller granulations cannot be detected. Cadaver data on their distribution are available [26], and areas of the arachnoid mater boundary can be assigned AG functionality in CFD simulations. Concretely, the AG can be assumed to act as one-way differential pressure valves with associated hydraulic conductivity of approximately 92.5 $\mu L\ min^{-1}\ mmHg^{-1}\ cm^{-2}$ [27].

Other drainage routes, namely drainage through lymphatic pathways, are clearly more difficult to model because there is no data available on local outflow rates and because, unlike the AG, no straightforward boundary condition can be implemented. This is not to say that those drainage pathways are unimportant: All drainage routes link the intracranial space and its dynamics with either the cardiovascular system or the lymphatic pathways. Increased pressure in either of these may reduce the reabsorption rate of CSF, thereby contributing to elevated intracranial pressure or hydrocephalus [28].

8.2.4 Calculating the Flow

Once the computational grid and the boundary conditions are in place, initial values of flow velocity and pressure have to be defined throughout the computational domain. Unless results of similar previous calculations exist from which initial conditions can be extra- or interpolated, zero pressure and velocity are usually assumed. Since the corresponding fluid dynamic state does not match to the actual flow field, transient calculations will have to be performed over a few cardiac (and, if considered, respiratory) cycles until no significant difference in the state between two subsequent cycles can be observed. Depending on the CFD solver used, a zero initial condition may render the calculations instable. In that case, the magnitudes or amplitudes of the applied boundary conditions can be scaled down initially and increased to their actual values over several cycles.

Steady-state calculations of arterial blood flow are quite common. While they do not capture all the details of the flow, their use can be justified if estimates of average wall shear stress distribution or other similar parameters linked to long-term processes such as atherosclerosis are to be studied [29]. In contrast to arterial blood flow, CSF flow has a much stronger pulsatile component compared to its net flow, which makes it more difficult to advocate steady-state simulations of cerebrospinal fluid dynamics. For transient CFD simulations, the proper temporal discretization step size has to be chosen, which will depend on the expected flow frequencies (see Sect. 8.2.3), the discretization scheme, the spatial resolution of the computational grid and the CFD solver. Commonly used time step sizes in the CSF space are on the order of 1 ms. As with the grid independence study (Sect. 8.2.2), time step independence of the acquired solution has to be ensured.

CSF is a Newtonian fluid with a viscosity of approximately 0.8 mPa s at 37°C that is fairly stable with respect to protein content, blood cell count and glucose concentration [30, 31]. In its entire domain, CSF flow is laminar and does not require any turbulence modeling. There are various CFD software frameworks and stand-alone solvers suitable for CSF flow calculations, and the decision in favor of the one or the

other will depend, to a large extent, on the background and preferences of the user. Despite the incompressibility of the cerebrospinal fluid, transient flow calculations in anatomically accurate, deforming representations of the CSF space demand substantial computer power. Consequently, CFD codes that support parallel processing on deforming grids with high scaling efficiency and without the need for manual partitioning should be preferred. Scaling efficiency generally decreases with increasing number of parallel processors used. The current trend in the development of computer hardware towards larger numbers of cores per CPU, but only slowly increasing clock speeds, is contributing to the rise of lattice Boltzmann (LB) CFD methods, where the discrete Boltzmann equation is solved instead of the Navier–Stokes equations [32]. LB codes scale better with increasing number of processors than classical NS solvers, and they are easier to implement on GPUs, which promise to deliver significant speed-ups compared to calculations on CPUs alone. High-end workstations running lattice Boltzmann codes on GPUs may be the most promising route for bringing CFD simulations of cerebrospinal fluid flow into the clinical environment.

8.3 Existing CFD Models

There are currently no CFD models that capture the CSF space in its entirety. Instead, the existing models focus on individual compartments or small groups of these. This section gives an overview of CFD models of the ventricular, subarachnoid and perivascular spaces.

8.3.1 Ventricular Space

The first CFD work on flow in the CSF space was the investigation of Jacobson and co-workers in 1996, where they investigated steady and oscillatory fluid dynamics through a representation of the aqueduct of Slylvius with stiff walls and reported (singularly considering net flow) that the aqueduct provides less than 5% of the total resistance to CSF flow within the CSF pathways [1]. The same authors followed up with an investigation of aqueduct stenosis in 1999. They approximated the geometry of the aqueduct of Sylvius based on published anatomic data and reported that a stenosis may increase the pressure drop across the aqueduct by two orders of magnitude compared to the physiological case [33]. Again, the aqueduct wall was considered to be stiff. Several years later, Fin and Grebe modeled the aqueduct wall as a deformable membrane and compared therewith obtained results to data attained with rigid walls [34]. The domain geometry was obtained via MRI and the CSF flow was solved using finite element and immersed boundaries methods. Under steady flow conditions, they obtained a 37% lower pressure drop in the case with deformable walls compared to rigid walls. This remarkable difference raises the question whether such a large influence of boundary conditions on the results does not diminish the value of CFD, as the actual aqueduct wall stiffness is not known. One may ask why the time and effort needed for CFD modeling should be invested

as opposed to the use of simple bulk models: Bulk models will be sufficient if bulk values such as the pressure drop across a simple structure are sought. If, however, one is interested in the effect of local geometric features on flow, CFD models will provide added value. To be clear, this still requires that the boundary conditions, which to a large extent determine the accuracy of the model, are as close as possible to the actual values that they represent.

After the CFD studies of the aqueduct of Sylvius, other researchers directed their efforts at the remainder of the ventricular space, using varying levels of detail in both the representation of the anatomy as well as in the acquisition of the boundary conditions. In 2005, my co-workers and I published results of simulations on a simplified representation of the entire ventricular space, within which CSF flow was driven by the expansion and contraction of the third ventricle walls [35]. While it is not known how exactly vascular deformation is translated to CSF motion, it is clear that this does not occur exclusively through the third ventricle as formerly suggested by Du Boulay [36]. The amplitude of the wall expansion was chosen such that a Reynolds number of ten was obtained in the aqueduct, as this corresponded to flow velocities reported in the literature. However, current MRI studies indicate that velocities should be up to a factor of five higher, which we also showed in a later study on CSF flow in an anatomically accurate representation of the third ventricle and the aqueduct of Sylvius [19]. In that study, the domain geometry was reconstructed based on MRI data. The ventricle wall motion in feet-head direction as well as the flow profile in the aqueduct of Sylvius was obtained as boundary conditions again via magnetic resonance imaging. The main finding was that the third ventricle displayed comparably complex flow with two mobile recirculation zones of different sizes generated by a jet emanating from the aqueduct of Sylvius. While a relatively high maximum Reynolds number of 340 was observed in the aqueduct, there were no indications of transitional or turbulent flow. In a follow-up paper, we investigated mass transport in the same domain [37]. We found that while in the center of the third ventricle transport is entirely convection-driven, the regions of the anterior and posterior recess show markedly lower Péclet numbers, indicating that mass transport through diffusion cannot be neglected there a priori. We further hypothesized that the characteristic shape of the third ventricle may facilitate endocrine communication between hypothalamus and pituitary gland through the CSF, which had been shown to occur in sheep [38]. In 2010, Cheng et al. investigated, also with an MRI-derived CFD model of the third ventricle and aqueduct of Sylvius, how the position of the interthalamic adhesion affects CSF flow [39]. They imposed flow at the foramina of Monro based on published values, set constant pressure at the distal end of the aqueduct and assumed rigid ventricle walls. The authors investigated four different positions of the interthalamic adhesion and found that the pressure in the third ventricle is higher when the adhesion is located close to the aqueduct. They went on to hypothesize that such morphologies with the adhesion in proximity of the aqueduct may have increased susceptibility to hydrocephalus if obstructions occur along the CSF flow pathway. As we did in our 2005 study [35], Cheng and co-workers relied on MRI flow data that underestimated velocities. It is likely that the stated main findings of their work would not change if higher velocities were considered. However, the detailed flow

fields and locations of recirculation zones would be different. In 2008, Howden and co-workers presented the first anatomically accurate 3D CFD model of the entire ventricular space [40]. Instead of using constant pressure boundary conditions at the domain outlets (the foramina of Luschka and Magendie), the authors applied transient pressure. This pressure curve was estimated using a geometrically simplified 3D model of the combined cranial and spinal CSF spaces that featured a pulsatile velocity inlet at the choroid plexus and constant pressure at the AG. While such a staggered approach is, in principle, preferable to using constant pressure, it is difficult to carry out in practice: The pulsation of the choroid plexus is not the sole origin of CSF oscillation, and the relative importance of the choroid plexus, ventricles and SAS as potential contributors to pulsatile flow is not known. The flow velocities at the boundaries reported by the simplified model were too low by a factor of two at minimum, and consequently, the validity of the entire flow and pressure field of the accurate model that depended on these boundary conditions was jeopardized. In 2011, Sweetman et al. proposed a model of the entire CSF space as an expansion of their previous 2D and 3D work on the cranial compartments [41–43]. The authors took a distinctly different approach than Howden et al., in that they prioritized the scope of the model over detail of the individual modules. While they included the SAS, they neglected its porous structure, which we had shown earlier to provide significant resistance to CSF flow [4]. To induce CSF pulsation, Sweetman et al. imposed a volume change in brain tissue that is transmitted to the fluid domain through deformable superior wall sections of the lateral ventricles. The temporal profile of the tissue volume change corresponded to measured basilar artery volumetric blood flow rate. The model displayed good agreement with spatially integrated MRI flow measurements at several locations. Given the wide range of possible tissue parameters, and in the absence of sensitivity tests with respect to these, the particular choice of values may be seen as a scaling factor to ensure global agreement between the computational model and the experimental results. This demonstrates a weakness of CFD models of CSF flow: MRI is used to acquire boundary conditions in areas where the corresponding measurements are possible, but MRI does not provide high enough effective resolution to validate the calculated flow field in detail. Hence, if CFD calculations are not carried out entirely wrong, there will be necessarily a global agreement of flows between the CFD and MRI data, but no statement can be made regarding the accuracy of the local flows. It is the ability to provide information on local flows that distinguishes CFD models from bulk models.

8.3.2 Subarachnoid Space

8.3.2.1 Spinal Subarachnoid Space

CFD models that focus on the SAS started in 2001 with the work of Loth et al. on CSF flow in the spinal canal [44]: the authors obtained a series of cross-sections of the spinal CSF space from imaging data of the Visual Human Project's Visible Man

[45] and set up a 2D model to assess the effects of spinal cord eccentricity and cross-sectional geometry on CSF flow. A 1D circular annulus model was further used to investigate the effects of flow area and cord motion. The substructure of the spinal canal including nerves and ligaments was not considered. Inertial effects were found to dominate the flow field under normal physiologic flow rates. A peak Reynolds number of 450 and Womersley number of up to 17 was observed. The authors suggested that a 3D model should be used to investigate secondary flows that are likely to occur in the cervical area, since lower dimensional models cannot capture these. In 2006, Stockman presented a 3D lattice Boltzmann model of a subsection of the spinal canal [46]. He was not concerned with obtaining the flow field (including secondary flows) along the entire spine, but rather with the effect of SAS substructure on CSF flow, which he investigated using a simplified geometry of the length of one vertebra. Stockman concluded that while the substructure has a limited effect on averaged CSF flow, it does influence the local flow field markedly. The limited effect on averaged flow is a somewhat surprising finding, as localized flow patterns such as re-circulations will dissipate energy, necessitating a larger axial pressure gradient to drive the flow. The same year, Bilston et al. presented a cylindrical 2D axisymmetric model of the spinal canal and cord to investigate whether a substantial CSF pressure increase could be induced by arachnoiditis in the SAS, which would support the hypothesis that syrinx formation in the spinal cord may be driven by CSF influx from the spinal canal [47]. The authors modeled arachnoiditis by defining a segment of the spinal canal as a porous medium region and performed finite-volume CFD calculations with prescribed temporal inflow profile based on MRI flow measurements at the superior end of the domain and a constant pressure boundary condition at the inferior end. They used the maximum calculated pressure as an input to a structural finite-element model of the spinal cord, obtained its deformations, updated the CFD model accordingly, and recalculated the pressure in the fluid domain. Depending on permeability and porosity of the porous region, CSF pressure was calculated to be 1–20 times higher than in the model without arachnoiditis, leading the authors to conclude that this elevated pressure may be involved in syrinx formation or enlargement. The authors cited the simplification of the domain geometry, the unknown structural characteristics of the arachnoiditis, as well as the linear elastic material properties used for the spinal cord as limitations of the study. In 2010, three CFD studies on CSF flow in the spinal SAS were published [48–50]. Among these, the work of Kuttler et al. on the analysis of drug distribution after intrathecal drug administration (i.e. drug delivery into the spinal SAS) was notable [50]. The authors generated a simplified 3D spinal domain based on data from the Visible Human Project [45] and imposed temporal flow profiles obtained via velocimetric MRI at the superior end of the domain. Lower-frequency CSF pulsation due to breathing was superimposed onto this flow by compression and decompression of the computational grid. The velocity field was calculated for one cardiac cycle and a steady streaming velocity field was derived therefrom (see [51] for a review on steady streaming). In order to obtain an initial drug distribution, a finer meshed domain of the lumbar and lower thoracic regions was generated, and drug administration as slow infusion or fast bolus injection was simulated using a turbulence model. The resulting drug concentration field was fed back into the larger scale model, where drug transport

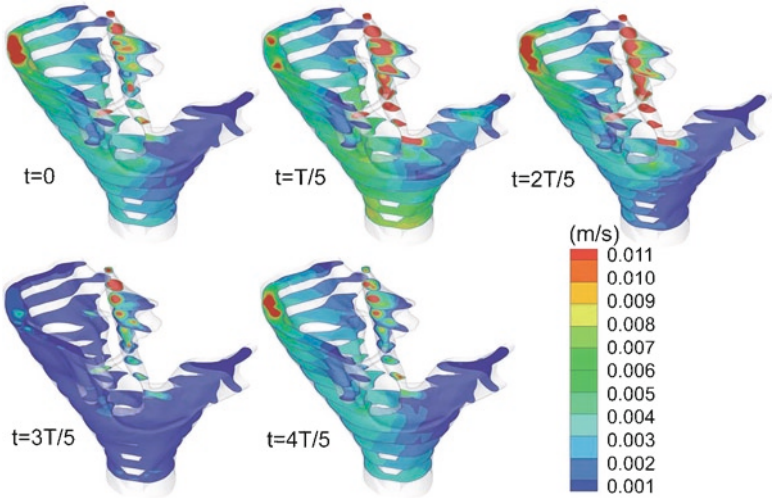

Fig. 8.5 Velocity magnitude contours during one complete cardiac cycle in the inferior cranial subarachnoid space according to our 2009 model [3]

was studied via the steady streaming field and diffusion modeling. The authors observed that there was no clear difference in the distribution range between bolus injection and slow infusion. More important than this result is the creative approach that Kuttler and co-workers showed in this study: By using different models for phenomena occurring at different time scales, they were able to progress towards a clinically relevant CFD application in the CSF space.

8.3.2.2 Cranial Subarachnoid Space

Some CFD models that include the cranial SAS were mentioned in Sect. 8.3.1 [41–43]. In a pair of papers published in 2009 and 2010, my group investigated flow in an anatomically accurate representation of a healthy cranial SAS and fourth ventricle [3, 4]. We imposed CSF flow velocities obtained through MRI at the pontine and cerebellomedullary cisterns and at the foramen magnum in the spinal canal. A constant pressure boundary condition was applied at the superior end of the fourth ventricle, and a mass source with zero initial momentum was introduced in the fourth ventricle to account for the production of CSF therein, whereas other production sources were included implicitly in the measured flow profiles. The SAS was modeled as an anisotropic homogeneous porous medium. CSF outflow was assumed to take place exclusively through AG, which were taken into account through a constant pressure boundary condition in the area of the superior sagittal sinus that did not allow for CSF reflux into the SAS. The domain boundaries were considered rigid. To ensure mass conservation, virtual CSF flux across the representation of the pia mater was allowed. We saw large variations in the spatial distribution of flow velocities (Figs. 8.5 and 8.6). Our main finding,

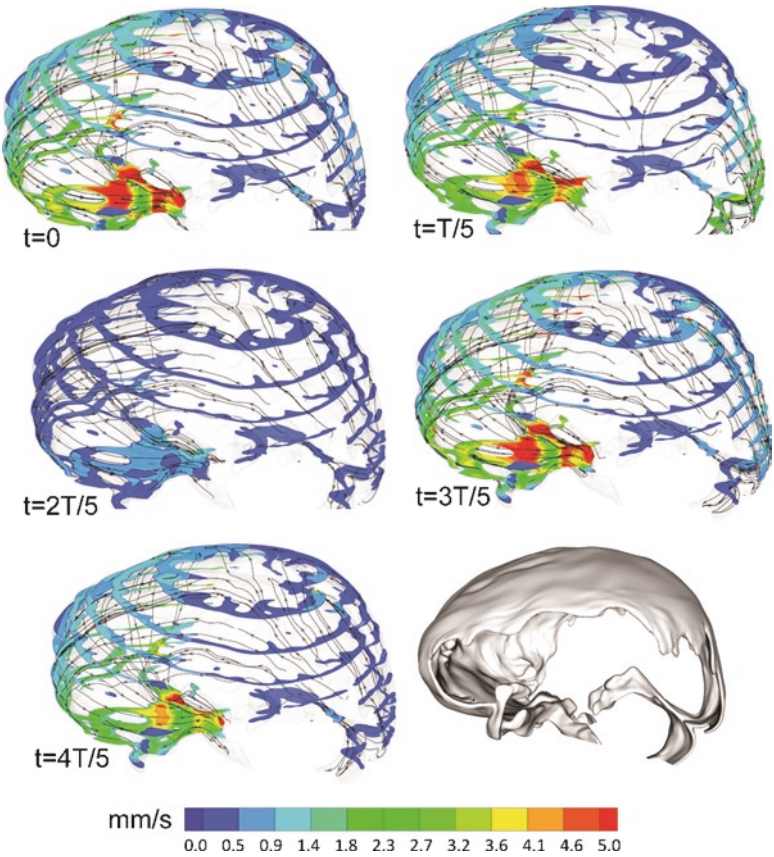

Fig. 8.6 Velocity magnitude contours at cross-sections in the superior cranial SAS at selected points in time within one cardiac cycle according to our 2010 model originally published in Gupta et al. [4]. Also shown are the stream traces of virtual massless particles injected arbitrarily within the domain at different points in time

however, was that the substructure of the SAS clearly contributes to the pressure drop across the domain, and that the characteristics of this structure need to be better quantified to allow for accurate flow computations.

8.3.3 Perivascular Space

Little work has been done thus far on modeling of perivascular flows. The first CFD study on this topic was published in 2003 by Bilston and co-workers [52]. They considered a 2D rectangular domain with no slip boundary conditions at the walls and prescribed pressures at inlet and outlet. Transient deformation was prescribed on the wall representing the boundary closer to the artery lumen. The outer wall was

considered rigid. The authors reported that fluid transport occurs in the direction of arterial wave propagation up to a specific pressure gradient determined by pulse wave velocity and amplitude. For the same conditions, Wang and Olbricht reported a lower maximal adverse pressure gradient based on a theoretical analysis against which fluid could be transported [53]. Using a different theoretical approach [59], demonstrated that fluid transport in the opposite direction of wave propagation could be possible under certain conditions. This reverse transport cannot occur in the model of Wang and Olbricht. In 2010, Bilston and co-workers expanded their original CFD model to take into account a time-varying pressure gradient along the perivascular domain, reflecting the pulsation of CSF in the SAS and showing that the relative timing of the arterial pulse wave and subarachnoid pressure wave could influence perivascular fluid flow [54].

8.4 Conclusion

CFD as such is not a novel method, but its history with regard to application in the cerebrospinal fluid space is comparably short. Most of the early CFD models of CSF dynamics placed emphasis on the development of the respective method rather than on answering specific questions. Results in the form of velocity and pressure data were produced almost as a by-product. Now that the basic CFD methodology is well defined, more emphasis needs to be placed on hypotheses to be tested. One could argue that detailed velocity and pressure fields provided by CFD are valuable by themselves without answering specific questions, since there is no other way of obtaining such spatially resolved data in a non-invasive manner. However, these raw data usually stay within the respective research group, providing no benefit to the scientific community as a whole. This is not to say that the development of CFD methods is obsolete, as major efforts are still needed in the description of cerebrospinal fluid flow without discounting the respective substructures and transient tissue deformations. Most importantly, coupling of the ventricular, subarachnoid, interstitial, vascular and perivascular fluid spaces needs to be achieved, and steps in this direction are being taken [55].

Given the reliance of CFD models on MRI for boundary conditions, the lack of agreement on key parameters such as the physiological flow rate in the aqueduct of Sylvius is a reason for concern: It is imperative that reference standards be established for commonly used CFD boundary conditions. Attention should be paid to the accuracy of data derived from MRI modalities that are comparably new with respect to their use in CFD models, such as elastography and diffusion tensor imaging [56]. When accurate boundary conditions are used, CFD is a well-established and reliable method for the investigation of fluid dynamics in the cerebral and spinal fluid spaces.

Acknowledgment Swiss National Science Foundation through SmartShunt – The Hydrocephalus Project.

References

1. Jacobson, E.E., Fletcher, D.F., Morgan, M.K., et al.: Fluid dynamics of the cerebral aqueduct. Pediatr. Neurosurg. **24**(5), 229–236 (1996)
2. Ballester, M.A.G., Zisserman, A., Brady, M.: Segmentation and measurement of brain structures in MRI including confidence bounds. Med. Image Anal. **4**(3), 189–200 (2000)
3. Gupta, S., Soellinger, M., Boesiger, P., et al.: Three-dimensional computational modeling of subject-specific cerebrospinal fluid flow in the subarachnoid space. J. Biomech. Eng. **131**(2), 021010 (2009). doi:10.1115/1.3005171
4. Gupta, S., Soellinger, M., Grzybowski, D.M., et al.: Cerebrospinal fluid dynamics in the human cranial subarachnoid space: an overlooked mediator of cerebral disease. I. Computational model. J. R. Soc. Interface **7**(49), 1195–1204 (2010). doi:rsif.2010.0033 [pii]10.1098/rsif.2010.0033
5. Allen, D.J., Low, F.N.: Scanning electron microscopy of the subarachnoid space in the dog. III. Cranial levels. J. Comp. Neurol. **161**(4), 515–539 (1975). doi:10.1002/cne.901610404
6. Cloyd, M.W., Low, F.N.: Scanning electron microscopy of the subarachnoid space in the dog. I. Spinal cord levels. J. Comp. Neurol. **153**(4), 325–368 (1974). doi:10.1002/cne.901530402
7. Killer, H.E., Laeng, H.R., Flammer, J., et al.: Architecture of arachnoid trabeculae, pillars, and septa in the subarachnoid space of the human optic nerve: anatomy and clinical considerations. Br. J. Ophthalmol. **87**(6), 777–781 (2003)
8. Vandenwesthuizen, J., Duplessis, J.P.: Quantification of unidirectional fiber bed permeability. J. Compos. Mater. **28**(7), 619–637 (1994)
9. Chai, Z.H., Shi, B.C., Lu, J.H., et al.: Non-Darcy flow in disordered porous media: a lattice Boltzmann study. Comput. Fluids **39**(10), 2069–2077 (2010). doi:10.1016/j.compfluid.2010.07.012
10. Kang, Q.J., Zhang, D.X., Chen, S.Y.: Unified lattice Boltzmann method for flow in multiscale porous media. Phys Rev E **66**(5), 056307 (2002). doi:10.1103/Physreve.66.056307
11. Lesage, D., Angelini, E.D., Bloch, I., et al.: A review of 3D vessel lumen segmentation techniques: models, features and extraction schemes. Med. Image Anal. **13**(6), 819–845 (2009). doi:10.1016/j.media.2009.07.011
12. Hjelle, Ø., Dæhlen, M.: Triangulations and Applications. Mathematics and Visualization. Springer, Berlin (2006)
13. De Boor, C.: A Practical Guide to Splines. Applied Mathematical Sciences, vol 27, Rev. edn. Springer, New York (2001)
14. Hadaczek, P., Yamashita, Y., Mirek, H., et al.: The "perivascular pump" driven by arterial pulsation is a powerful mechanism for the distribution of therapeutic molecules within the brain. Mol. Ther. **14**(1), 69–78 (2006). doi:S1525-0016(06)00113-4[pii]10.1016/j.ymthe.2006.02.018
15. Mittal, R., Iaccarino, G.: Immersed boundary methods. Annu. Rev. Fluid Mech. **37**, 239–261 (2005). doi:10.1146/annurev.fluid.37.061903.175743
16. Spiegel, M., Redel, T., Zhang, Y.J., et al.: Tetrahedral vs. polyhedral mesh size evaluation on flow velocity and wall shear stress for cerebral hemodynamic simulation. Comput. Meth. Biomech. Biomed. Eng. **14**(1), 9–22 (2011). doi:10.1080/10255842.2010.518565
17. Haslam, M., Zamir, M.: Pulsatile flow in tubes of elliptic gross sections. Ann. Biomed. Eng. **26**(5), 780–787 (1998)
18. Gupta, S., Poulikakos, D., Kurtcuoglu, V.: Analytical solution for pulsatile viscous flow in a straight elliptic annulus and application to the motion of the cerebrospinal fluid. Phys. Fluids **20**(9), 093607 (2008). doi:10.1063/1.2988858
19. Kurtcuoglu, V., Soellinger, M., Summers, P., et al.: Computational investigation of subject-specific cerebrospinal fluid flow in the third ventricle and aqueduct of Sylvius. J. Biomech. **40**(6), 1235–1245 (2007). doi:S0021-9290(06)00215-6[pii]10.1016/j.jbiomech.2006.05.031
20. Boutsianis, E., Gupta, S., Boomsma, K., et al.: Boundary conditions by Schwarz-Christoffel mapping in anatomically accurate hemodynamics. Ann. Biomed. Eng. **36**(12), 2068–2084 (2008). doi:10.1007/s10439-008-9571-3

21. Soellinger, M., Rutz, A.K., Kozerke, S., et al.: 3D cine displacement-encoded MRI of pulsatile brain motion. Magn. Reson. Med. **61**(1), 153–162 (2009). doi:10.1002/mrm.21802
22. Shannon, C.E.: Communication in the presence of noise. Proc. Inst. Radio Eng. **37**(1), 10–21 (1949)
23. Luke, H.D.: The origins of the sampling theorem. IEEE Commun. Mag. **37**(4), 106–108 (1999)
24. Greitz, D., Greitz, T., Hindmarsh, T.: A new view on the CSF-circulation with the potential for pharmacological treatment of childhood hydrocephalus. Acta Paediatr. **86**(2), 125–132 (1997)
25. Koh, L., Zakharov, A., Johnston, M.: Integration of the subarachnoid space and lymphatics: is it time to embrace a new concept of cerebrospinal fluid absorption? Cerebrospinal Fluid Res. **2**, 6 (2005). doi:10.1186/1743-8454-2-6
26. Grzybowski, D.M., Herderick, E.E., Kapoor, K.G., et al.: Human arachnoid granulations. Part I: a technique for quantifying area and distribution on the superior surface of the cerebral cortex. Cerebrospinal Fluid Res. **4**, 6 (2007). doi:10.1186/1743-8454-4-6
27. Holman, D.W., Kurtcuoglu, V., Grzybowski, D.M.: Cerebrospinal fluid dynamics in the human cranial subarachnoid space: an overlooked mediator of cerebral disease. II. In vitro arachnoid outflow model. J. R. Soc. Interface **7**(49), 1205–1218 (2010). doi:rsif.2010.0032 [pii]10.1098/rsif.2010.0032
28. Bateman, G.: Hyperemic hydrocephalus: a new form of childhood hydrocephalus analogous to hyperemic intracranial hypertension in adults. J. Neurosurg. Pediatr. **5**(1), 20–26 (2010). doi:10.3171/2009.8.PEDS09204
29. Knight, J., Olgac, U., Saur, S.C., et al.: Choosing the optimal wall shear parameter for the prediction of plaque location-A patient-specific computational study in human right coronary arteries. Atherosclerosis **211**(2), 445–450 (2010). doi:10.1016/j.atherosclerosis.2010.03.001
30. Bloomfield, I.G., Johnston, I.H., Bilston, L.E.: Effects of proteins, blood cells and glucose on the viscosity of cerebrospinal fluid. Pediatr. Neurosurg. **28**(5), 246–251 (1998)
31. Brydon, H.L., Hayward, R., Harkness, W., et al.: Physical properties of cerebrospinal fluid of relevance to shunt function. 1: the effect of protein upon CSF viscosity. Br. J. Neurosurg. **9**(5), 639–644 (1995)
32. Chen, S., Doolen, G.D.: Lattice Boltzmann method for fluid flows. Annu. Rev. Fluid Mech. **30**, 329–364 (1998)
33. Jacobson, E.E., Fletcher, D.F., Morgan, M.K., et al.: Computer modelling of the cerebrospinal fluid flow dynamics of aqueduct stenosis. Med. Biol. Eng. Comput. **37**(1), 59–63 (1999)
34. Fin, L., Grebe, R.: Three dimensional modeling of the cerebrospinal fluid dynamics and brain interactions in the aqueduct of sylvius. Comput. Methods Biomech. Biomed. Engin. **6**(3), 163–170 (2003). doi:10.1080/1025584031000097933016C8J55KCLQF4JT[pii]
35. Kurtcuoglu, V., Poulikakos, D., Ventikos, Y.: Computational modeling of the mechanical behavior of the cerebrospinal fluid system. J. Biomech. Eng. **127**(2), 264–269 (2005)
36. Du Boulay, G., O'Connell, J., Currie, J., et al.: Further investigations on pulsatile movements in the cerebrospinal fluid pathways. Acta Radiol. Diagn. (Stockh) **13**, 496–523 (1972)
37. Kurtcuoglu, V., Soellinger, M., Summers, P., et al.: Mixing and modes of mass transfer in the third cerebral ventricle: a computational analysis. J. Biomech. Eng. **129**(5), 695–702 (2007). doi:10.1115/1.2768376
38. Tricoire, H., Locatelli, A., Chemineau, P., et al.: Melatonin enters the cerebrospinal fluid through the pineal recess. Endocrinology **143**(1), 84–90 (2002)
39. Cheng, S., Tan, K., Bilston, L.E.: The effects of the interthalamic adhesion position on cerebrospinal fluid dynamics in the cerebral ventricles. J. Biomech. **43**(3), 579–582 (2010). doi:S0021-9290(09)00566-1[pii]10.1016/j.jbiomech.2009.10.002
40. Howden, L., Giddings, D., Power, H., et al.: Three-dimensional cerebrospinal fluid flow within the human ventricular system. Comput. Methods Biomech. Biomed. Engin. **11**(2), 123–133 (2008). doi:785046036[pii]10.1080/10255840701492118
41. Linninger, A.A., Xenos, M., Zhu, D.C., et al.: Cerebrospinal fluid flow in the normal and hydrocephalic human brain. IEEE Trans. Biomed. Eng. **54**(2), 291–302 (2007). doi:10.1109/TBME.2006.886853
42. Sweetman, B., Linninger, A.A.: Cerebrospinal fluid flow dynamics in the central nervous system. Ann. Biomed. Eng. **39**(1), 484–496 (2011). doi:10.1007/s10439-010-0141-0

43. Sweetman, B., Xenos, M., Zitella, L., et al.: Three-dimensional computational prediction of cerebrospinal fluid flow in the human brain. Comput. Biol. Med. **41**(2), 67–75 (2011). doi:10.1016/j.compbiomed.2010.12.001
44. Loth, F., Yardimci, M.A., Alperin, N.: Hydrodynamic modeling of cerebrospinal fluid motion within the spinal cavity. J. Biomech. Eng. **123**(1), 71–79 (2001)
45. The Visible Human Project. 1997. http://www.nlm.nih.gov/research/visible/visible_human.html. Accessed February 2011
46. Stockman, H.W.: Effect of anatomical fine structure on the flow of cerebrospinal fluid in the spinal subarachnoid space. J. Biomech. Eng. **128**(1), 106–114 (2006)
47. Bilston, L.E., Fletcher, D.F., Stoodley, M.A.: Focal spinal arachnoiditis increases subarachnoid space pressure: a computational study. Clin. Biomech. (Bristol, Avon) **21**(6), 579–584 (2006)
48. Hentschel, S., Mardal, K.A., Lovgren, A.E., et al.: Characterization of cyclic CSF flow in the foramen magnum and upper cervical spinal canal with MR flow imaging and computational fluid dynamics. AJNR Am. J. Neuroradiol. **31**(6), 997–1002 (2010). doi:ajnr.A1995 [pii] 10.3174/ajnr.A1995
49. Linge, S.O., Haughton, V., Lovgren, A.E., et al.: CSF flow dynamics at the craniovertebral junction studied with an idealized model of the subarachnoid space and computational flow analysis. AJNR Am. J. Neuroradiol. **31**(1), 185–192 (2010). doi:ajnr.A1766 [pii] 10.3174/ajnr.A1766
50. Kuttler, A., Dimke, T., Kern, S., et al.: Understanding pharmacokinetics using realistic computational models of fluid dynamics: biosimulation of drug distribution within the CSF space for intrathecal drugs. J. Pharmacokinet. Pharmacodyn. **37**(6), 629–644 (2010). doi:10.1007/s10928-010-9184-y
51. Riley, N.: Steady streaming. Annu. Rev. Fluid Mech. **33**, 43–65 (2001)
52. Bilston, L.E., Fletcher, D.F., Brodbelt, A.R., et al.: Arterial pulsation-driven cerebrospinal fluid flow in the perivascular space: a computational model. Comput. Methods Biomech. Biomed. Engin. **6**(4), 235–241 (2003)
53. Wang, P., Olbricht, W.L.: Fluid mechanics in the perivascular space. J. Theor. Biol. (2011). doi:10.1016/j.jtbi.2011.01.014
54. Bilston, L.E., Stoodley, M.A., Fletcher, D.F.: The influence of the relative timing of arterial and subarachnoid space pulse waves on spinal perivascular cerebrospinal fluid flow as a possible factor in syrinx development. J. Neurosurg. **112**(4), 808–813 (2010). doi:10.3171/2009.5.JNS08945
55. Tully, B., Ventikos, Y.: Coupling poroelasticity and CFD for cerebrospinal fluid hydrodynamics. IEEE Trans. Biomed. Eng. **56**(6), 1644–1651 (2009). doi:10.1109/TBME.2009.2016427
56. Sarntinoranont, M., Chen, X., Zhao, J., et al.: Computational model of interstitial transport in the spinal cord using diffusion tensor imaging. Ann. Biomed. Eng. **34**(8), 1304–1321 (2006). doi:10.1007/s10439-006-9135-3
57. Tillmann, B.: Atlas der Anatomie des Menschen. Springer, Berlin (2005)
58. Schmid Daners, M., Knobloch, V., Soellinger, M., et al.: Age-specific characteristics and coupling of cerebral arterial inflow and cerebrospinal fluid dynamics (2011)
59. Schley, D., Carare-Nnadi, R., Please, C.P., et al.: Mechanisms to explain the reverse perivascular transport of solutes out of the brain. J Theor Biol. **238**(4), 962–974 (2006). doi:10.1016/j.jtbi.2005.07.005